

Letter

Detection of nitrogen and oxygen in a galaxy at the end of reionization

Ken-ichi TADAKI^{1,2,*}, Akiyoshi TSUJITA³, Yoichi TAMURA⁴, Kotaro KOHNO^{3,5}, Bunyo HATSUKADE³, Daisuke IONO^{1,2}, Minju M. LEE^{6,7}, Yuichi MATSUDA^{1,2}, Tomonari MICHİYAMA^{1,8}, Tohru NAGAO⁹, Kouichiro NAKANISHI^{1,2}, Yuri NISHIMURA^{1,3}, Toshiki SAITO^{1,10}, Hideki UMEHATA^{3,11} and Jorge ZAVALA¹

¹National Astronomical Observatory of Japan, 2-21-1 Osawa, Mitaka, Tokyo 181-8588, Japan

²Department of Astronomical Science, SOKENDAI (The Graduate University for Advanced Studies), Mitaka, Tokyo 181-8588, Japan

³Institute of Astronomy, Graduate School of Science, The University of Tokyo, 2-21-1 Osawa, Mitaka, Tokyo 181-0015, Japan

⁴Division of Particle and Astrophysical Science, Nagoya University, Furocho, Chikusa, Nagoya 464-8602, Japan

⁵Research Center for the Early Universe, Graduate School of Science, The University of Tokyo, 7-3-1 Hongo, Bunkyo-ku, Tokyo 113-0033, Japan

⁶Cosmic Dawn Center (DAWN), Jagtvej 128, DK-2200 Copenhagen N, Denmark

⁷DTU-Space, Technical University of Denmark, Elektrovej 327, DK2800 Kgs. Lyngby, Denmark

⁸Department of Earth and Space Science, Osaka University, 1-1 Machikaneyama, Toyonaka, Osaka 560-0043, Japan

⁹Research Center for Space and Cosmic Evolution, Ehime University, Matsuyama, Ehime 790-8577, Japan

¹⁰Department of Physics, General Studies, College of Engineering, Nihon University, 1 Nakagawara, Tokusada, Tamuramachi, Koriyama, Fukushima 963-8642, Japan

¹¹Institute for Cosmic Ray Research, The University of Tokyo, 5-1-5 Kashiwanoha, Kashiwa, Chiba 277-8582, Japan

*E-mail: tadaki.ken@nao.ac.jp

Received (reception date); Accepted (acceptation date)

Abstract

We present observations of [N II] 205 μm , [O III] 88 μm and dust emission in a strongly-lensed, submillimeter galaxy (SMG) at $z = 6.0$, G09.83808, with the Atacama Large Millimeter/submillimeter Array (ALMA). Both [N II] and [O III] line emissions are detected at $> 12\sigma$ in the 0.8''-resolution maps. Lens modeling indicates that the spatial distribution of the dust continuum emission is well characterized by a compact disk with an effective radius of 0.64 ± 0.02 kpc and a high infrared surface brightness of $\Sigma_{\text{IR}} = (1.8 \pm 0.3) \times 10^{12} L_{\odot} \text{ kpc}^{-2}$. This result supports that G09.83808 is the progenitors of compact quiescent galaxies at $z \sim 4$,

where the majority of its stars are expected to be formed through a strong and short burst of star formation. G09.83808 and other lensed SMGs show a decreasing trend of the [N II] line to infrared luminosity ratio with increasing continuum flux density ratio between 63 μm and 158 μm , as seen in local luminous infrared galaxies (LIRGs). The decreasing trend can be reproduced by photoionization models with increasing ionization parameters. Furthermore, by combining the [N II]/[O III] luminosity ratio with far-infrared continuum flux density ratio in G09.83808, we infer that the gas phase metallicity is already $Z \approx 0.5 - 0.7 Z_{\odot}$. G09.83808 is likely one of the earliest galaxies that has been chemically enriched at the end of reionization.

Key words: galaxies: high-redshift — galaxies: starburst — galaxies: ISM

1 Introduction

The most massive galaxies form earliest in the Universe, known as downsizing of galaxy formation (e.g., Cowie et al. 1996, Thomas et al. 2010). This naturally motivates us to explore massive mature galaxies at the highest redshift. The current record redshift of spectroscopically confirmed quiescent galaxies (QGs) is $z = 4.01$ (Tanaka et al. 2019) and many QGs have been identified at $z = 3 - 4$ (e.g., Schreiber et al. 2018). They are extremely compact in the rest-frame optical with an effective radius of less than 1 kpc (e.g., Kubo et al. 2018). The compact stellar distribution could be related to bursty star formation histories with star formation rate (SFR) of several hundreds $M_{\odot}\text{yr}^{-1}$ in the center, as implied by near-infrared spectroscopic studies (e.g., Glazebrook et al. 2017, Valentino et al. 2020). These findings suggest that starburst galaxies at $z = 5 - 7$ such as bright submillimeter galaxies (SMGs) are good candidates for the progenitors of massive QGs at $z = 3 - 4$ (see also Toft et al. 2014; Ikarashi et al. 2015).

For understanding how the most massive galaxies grow in such an early universe, we study the star-forming activities and the physical conditions in the interstellar medium (ISM) of a strongly-lensed SMG at $z = 6.027$, G09.83808 (Zavala et al. 2018). G09.83808 is one of three bright SMGs so far discovered at $z > 6$, and is a more common populations of starburst galaxies with the intrinsic 870 μm flux density of $S_{870,\text{intr}} \sim 4$ mJy, compared to the other two extreme ones with $S_{870,\text{intr}} > 10$ mJy (Riechers et al. 2013; Marrone et al. 2018). In this work, we focus on the far-infrared fine structure lines of nitrogen [N II]₂₀₅ and oxygen [O III]₈₈. Nitrogen line emission is especially important for understanding the chemical evolution of galaxies because nitrogen is mainly produced from carbon and oxygen already present in stars through the CNO cycle, referred to as secondary element (e.g., Kobayashi et al. 2020). Nitrogen is formed in intermediate-mass stars which are longer-lived than massive stars, inducing a time-delay. Thus, an enhanced

ratio between [N II]₂₀₅ and [O III]₈₈ luminosity implies that galaxies experienced many cycles of star formation. Recent ALMA observations have detected nitrogen lines ([N II]₂₀₅ or [N II]₁₂₂) in galaxies at $z \sim 5$ (e.g., Pavesi et al. 2019, Cunningham et al. 2020). But galaxies where both nitrogen and oxygen lines are detected are limited to $z < 5$ (De Breuck et al. 2019; Tadaki et al. 2019), except for bright quasars (Novak et al. 2019; Li et al. 2020). For pushing studies of ISM in starburst galaxies to higher redshift, we observe the [O III]₈₈ line emission ($\nu_{\text{obs}}=482.9$ GHz) and [N II]₂₀₅ ($\nu_{\text{obs}}=207.9$ GHz), as well as the 0.6 mm and 1.5 mm continuum emission, in G09.83808.

2 Observations

ALMA observations were executed on 2019 December (Band-8) and 2019 October–2020 January (Band-5). On-source time was 2.4 h and 1.6 h, respectively. The maximum recovery scale is 5'4 and 6'2, respectively. The data were calibrated in the standard manner using CASA (McMullin et al. 2007). We first construct a clean mask with the 0.6 mm continuum data by applying CASA/AUTO-MULTITHRESH (Kepley et al. 2020) and Briggs weighting with robust=+0.5. We use this mask for all imaging of continuum and line emission. Then, we clean the emission down to the 1.5σ level to create continuum and 100 km s⁻¹ channel maps with robust=-0.5 and robust=+2.0, respectively. Figure 1 shows the ALMA maps of the 0.6 mm, 1.5 mm continuum, [O III]₈₈ and [N II]₂₀₅ line emission in G09.83808, where two arcs of counter-images are evident. The line emission is integrated over the velocity range of -350 km s⁻¹ to $+150$ km s⁻¹. The beam size is 0'56×0'38 for the 0.6 mm continuum, 0'48×0'41 for the 1.5 mm continuum, 0'76×0'64 for the [O III]₈₈, and 0'84×0'77 for the [N II]₂₀₅ line map. The peak flux densities and noise levels are 7.46 ± 0.17 mJy beam⁻¹ (44σ) for the 0.6 mm continuum, 2.10 ± 0.03 mJy beam⁻¹ (75σ) for the 1.5 mm continuum, 1.59 ± 0.12 Jy km s⁻¹ beam⁻¹ (14σ) for the [O III]₈₈, and 0.38 ± 0.03 Jy km

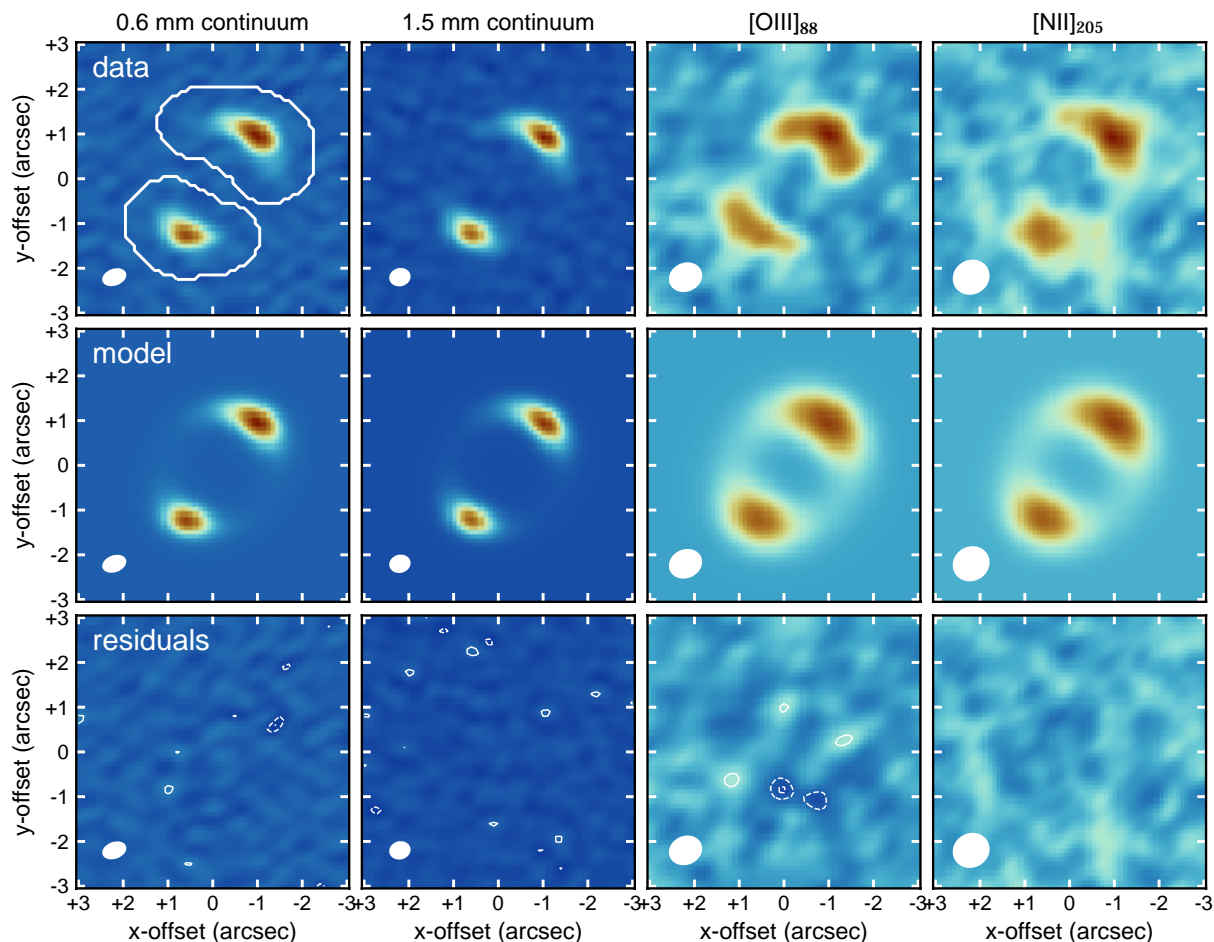


Fig. 1. Top: from left to right, the ALMA maps of 0.6 mm, 1.5 mm continuum, [O III]₈₈ and [N II]₂₀₅ line emission are displayed. The mask region is shown in the top left panel. Middle and bottom panels show the best-fit models produced by GLAFIC and the residuals, respectively. White dashed and solid contours show the -4σ , -3σ and $+3\sigma$, $+4\sigma$ levels in the residual maps. We use a scientific color scale from Crameri et al. (2020).

$s^{-1} \text{ beam}^{-1}$ (12σ) for the [N II]₂₀₅ line map. The total flux densities and line fluxes in the mask region are 38.69 ± 1.13 mJy for the 0.6 mm continuum, 9.91 ± 0.19 mJy for the 1.5 mm continuum, 8.13 ± 0.50 Jy km s⁻¹ for the [O III]₈₈, and 1.48 ± 0.12 Jy km s⁻¹ for the [N II]₂₀₅ line map. The uncertainties are calculated as $1\sigma \times \sqrt{(N_{\text{mask}}/N_{\text{beam}})}$ where N_{mask} and N_{beam} is the areas of the mask region and the clean beam, respectively.

3 Analysis and results

3.1 Gravitational lens modeling

Strong gravitational lensing produces multiple images of a background source, G09.83808 at $z = 6.027$, in the ALMA maps. A big advantage of submillimeter observations is that the flux contribution of a foreground source, a massive quiescent galaxy at $z = 0.776$ (Fudamoto et al. 2017), is negligible in this wavelength unlike optical and near-

infrared observations. For mass models of foreground (lens) source, we assume a singular isothermal ellipsoid with five parameters (xy -coordinates, ellipticity e , position angle measured counterclockwise from North θ_e , velocity dispersion σ_v) and external perturbation with two parameters (tidal shear γ and position angle θ_γ) in a similar way as in Tamura et al. (2015). The background source is assumed to have an exponential disk with a Sérsic index of $n = 1$, characterized by six parameters (xy -coordinates, flux, effective radius R_{eff} , major-to-minor axis ratio q and position angle θ_q), for both the continuum and line emissions.

First, we determine the parameters of the foreground source by using the 1.5 mm continuum image, where the spatial resolution and signal-to-noise ratio are better than those of other images. We then use GLAFIC2 software (Oguri 2010) to optimize the mass model of the foreground source. Only the clean mask region is used for χ^2 minimization. To estimate the uncertainties of the best-

fit parameters, we add a 1σ noise map convolved by a dirty beam to the clean image and repeat to fit the noise added images. The best-fit parameters are $e = 0.11^{+0.02}_{-0.08}$, $\theta_e = 78^{+33}_{-3}$ deg, $\sigma_v = 257.9^{+0.3}_{-2.0}$ km s $^{-1}$ for an isothermal ellipsoid and $\gamma = 4.1^{+2.8}_{-0.0} \times 10^{-2}$ and $\theta_\gamma = 47^{+11}_{-3}$ deg for an external shear. The uncertainties are based on the 16th and 84th percentile of 500 MonteCarlo runs. The derived position of the foreground source is nicely consistent with the position in a deep z-band image ($0''.7$ seeing) from the second public data release of the Hyper Suprime-Cam in Subaru Strategic Program (Aihara et al. 2019).

We also obtain the central position and the shape of the 1.5 mm continuum emission for the background source. The spatial distribution is well characterized by an exponential disk with $q = 0.93^{+0.02}_{-0.08}$ and $\theta_q = 108^{+13}_{-22}$ deg. Even if n is a free parameter, the best-fit value is $n = 1.17^{+0.13}_{-0.10}$, supporting that the dust continuum emission has an exponential profile (Hodge et al. 2016; Fujimoto et al. 2018). The total magnification factor, given by a ratio between flux densities in the image and source plane, is $\mu = 8.38^{+0.74}_{-0.27}$, which is consistent with the previous result from $0''.1$ -resolution observations of $870 \mu\text{m}$ continuum emission ($\mu = 9.3 \pm 1.0$; Zavala et al. 2018).

Next, we measure the intrinsic sizes of the continuum and line emissions for the background source by fixing the other parameters to the values obtained above. The effective radii are $0''.112^{+0.002}_{-0.002}$ for the 1.5 mm continuum, $0''.117^{+0.004}_{-0.003}$ for the 0.6 mm continuum, $0''.21^{+0.08}_{-0.08}$ for the $[\text{O III}]_{88}$ and $0''.20^{+0.04}_{-0.04}$ for the $[\text{N II}]_{205}$ line emission. The dust emissions at different wavelength have a similar size and both are more compact than the ionized gas emissions.

Figure 1 shows the best-fit model and residuals for each emission. The residual image of $[\text{O III}]_{88}$ emission shows three $+3\sigma$ peaks in the edges of the two arcs, corresponding to the direction of the minor axis of the disk component in the source plane. Even if the position angle is not fixed, the 3σ residuals still remain. Given that the emission peak is detected at 12σ , the 3σ deviation from an exponential disk may suggest that G09.83808 has subcomponents (clumps or small satellite galaxies) of ionized gas. We require deeper and higher-resolution observations to confirm the existence of these components.

3.2 Dust SED modeling

Combining the new ALMA continuum data with photometry from Herschel, JCMT, and LMT observations (Ivison et al. 2016; Fudamoto et al. 2017; Zavala et al. 2018), we constrain the spectral energy distribution (SED) of dust emission to estimate the total infrared luminosity,

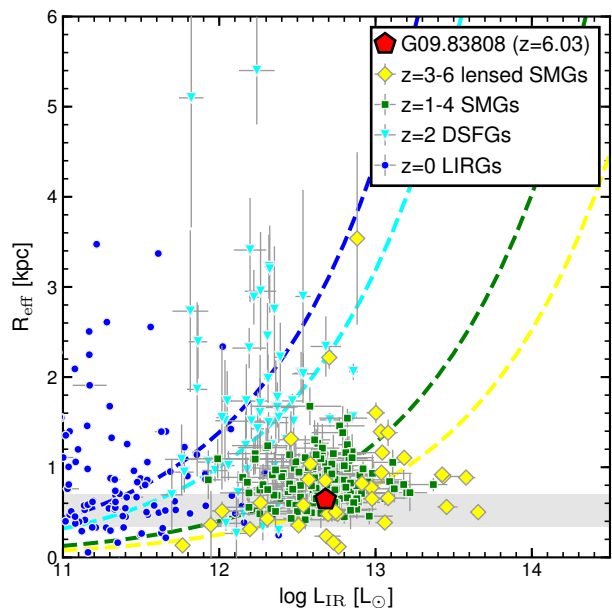


Fig. 2. Intrinsic infrared luminosities versus circularized effective radii for G09.83808 at $z=6$, strongly-lensed SMGs (Spilker et al. 2016), SMGs at $z = 1 - 4$ (Gullberg et al. 2019; Dudzevičiūtė et al. 2020), DSFGs at $z = 2$ (Tadaki et al. 2020) and LIRGs at $z = 0$ (Lutz et al. 2016). A shaded region shows the effective radius of the rest-frame optical emission in massive quiescent galaxies at $z \sim 4$ (Kubo et al. 2018). Dashed lines correspond to the median values of the infrared surface densities for each sample.

L_{IR} . We assume flux calibration uncertainties of 5% and 10% in ALMA Band-5 and Band-8 observations. We fit a modified blackbody radiation model, characterized by dust temperature T_{dust} and an emissivity index β (Casey et al. 2012), to the observed SEDs by using the CIGALE code (Boquien et al. 2019). We fix the wavelength where the optical depth is unity to $150 \mu\text{m}$ and the power law slope to 2.0. The best-fit model gives the total infrared luminosity between 8 and $1000 \mu\text{m}$ of $L_{\text{IR}} = (4.6^{+0.6}_{-0.7}) \times 10^{12} L_{\odot}$ after correction of magnification effect, $T_{\text{dust}} = 51 \pm 4$ K, and $\beta = 2.5^{+0.3}_{-0.2}$. As the 0.6 mm continuum emission corresponds to the peak of the dust SED, its spatial distribution probes where stars are intensively formed. We find G09.83808 to have an infrared surface density of $\Sigma_{\text{IR}} = (1.8 \pm 0.3) \times 10^{12} L_{\odot} \text{ kpc}^{-2}$ within the circularized effective radius, $R_{\text{eff},0.6\text{mm}} = 0.64 \pm 0.02$ kpc.

We also estimate the total infrared luminosities for other strongly lensed SMGs, where the $870 \mu\text{m}$ continuum sizes and magnification are measured (Weiß et al. 2013; Strandet et al. 2016; Spilker et al. 2016) in the same way as in G09.83808. Figure 2 shows the total infrared luminosity and circularized effective radius of dust continuum emission for four different galaxy populations: 1) strongly-lensed SMGs at $z = 3 - 6$ including G09.83808, 2) SMGs at $z = 1 - 4$ (Gullberg et al. 2019; Dudzevičiūtė

et al. 2020), 3) massive dusty star-forming galaxies at $z = 2$ (DSFGs; Tadaki et al. 2020), and 4) LIRGs at $z = 0$ (Lutz et al. 2016). The four populations occupy different regions in the $L_{\text{IR}} - R_{\text{eff}}$ plane. For any combination of the two populations, a KS test shows that the probability that they are drawn from the same distribution is less than 1%. The median values of the infrared surface densities are $2.5 \times 10^{12} L_{\odot} \text{ kpc}^{-2}$ for lensed SMGs, $1.0 \times 10^{12} L_{\odot} \text{ kpc}^{-2}$ for SMGs, $1.6 \times 10^{11} L_{\odot} \text{ kpc}^{-2}$ for DSFGs, and $0.8 \times 10^{11} L_{\odot} \text{ kpc}^{-2}$ for LIRGs. Thus, lensed SMGs and SMGs are undergoing intense starburst with a higher infrared surface density, compared to LIRGs and DSFGs. The small difference between lensed SMGs and SMGs may be due to the different redshift range (i.e. emissions at different rest-frame wavelengths) and/or a large magnification near caustics of gravitational lenses in extremely bright objects with $S_{1.4 \text{ mm}} > 20 \text{ mJy}$ (Weiß et al. 2013). The effective radii of lensed SMGs are comparable to those of massive QGs at $z \sim 4$ ($0.52 \pm 0.18 \text{ kpc}$ in the rest-frame optical; Kubo et al. 2018). The intense starburst in the central compact region supports an evolutionary link between G09.83808 at $z = 6$ and massive QGs at $z \sim 4$.

4 Far-infrared line properties

UV photons from massive stars ionize the surrounding gas and at the same time heat the dust. Then, thermal radiation of the dust can be observed in the infrared. A combination of fine structure lines such as $[\text{N II}]_{205}$ and $[\text{O III}]_{88}$ with infrared continuum emission can therefore provide with information about physical properties of the ISM and ionizing sources (e.g., metallicity, gas density and ionization parameter) in galaxies. We compare the line-to-infrared luminosity ratio, $L_{[\text{NII}]205}/L_{\text{IR}}$ and $L_{[\text{OIII}]88}/L_{\text{IR}}$, in G09.83808 and other lensed SMGs at $z = 3 - 6$ with those in local LIRGs. Although the spatial distributions of ionized gas and dust are different, we use the galaxy-integrated properties for straightforward comparison.

4.1 Nitrogen line emission

Herschel observations of $[\text{N II}]_{205}$ line in LIRGs at $z \sim 0$ show that $L_{[\text{NII}]205}/L_{\text{IR}}$ is anticorrelated with the continuum flux density ratio between $63 \mu\text{m}$ and $158 \mu\text{m}$, S_{63}/S_{158} (Díaz-Santos et al. 2017; Lu et al. 2017). For lensed SMGs, we derive S_{63}/S_{158} from the best-fit SED (section 3.2). In both galaxy populations, there is a decreasing trend of $L_{[\text{NII}]205}/L_{\text{IR}}$ with increasing S_{63}/S_{158} (Figure 3). The trends could be related to a variation in ionization parameter, defined as $U_{\text{ion}} = \phi(H)/c/n_H$

where $\phi(H)$ is the flux of hydrogen-ionizing photons, n_H is the hydrogen density at the illuminated face of a cloud, and c is the light speed. We use photoionization code *CLOUDY v17.01* (Ferland et al. 2017) to compare the observations with models with different ionization parameters. We generate the input spectra of a single age starburst model with 20 Myr by using the Binary Population and Spectral Synthesis (BPASS v2.0) code (Eldridge & Stanway 2016). The initial gas density at illuminated face is fixed to be $n_H = 50 \text{ cm}^{-3}$, which is the typical value in local LIRGs (Díaz-Santos et al. 2017). We adopt solar elemental abundance ratios and gas-phase depletion factors, with taking into account secondary production of nitrogen (Nagao et al. 2011) and assume a solar metallicity. For dust, we assume Orion-type graphite and silicate grains with a size distribution and abundance appropriate for those along the line of sight to the Trapezium stars in Orion. We stop calculations at the total hydrogen column density of $N(H) = 10^{22} \text{ cm}^{-2}$ to avoid the dust temperature becoming too low. We here do not intend to determine each parameters from fitting, but aim to interpret the observed trends from comparison with models.

The decreasing trend of $L_{[\text{NII}]205}/L_{\text{IR}}$ is successfully reproduced by photoionization models in the range of $U_{\text{ion}} = 10^{-4} - 10^{-2}$ (Figure 3). As an ionization parameter becomes larger, the H^+ region expands. But the volume of H^+ region does not increase linearly with U_{ion} because UV photon in turn is used to heat the dust in the expanded H^+ region (Abel et al. 2009). The fraction of UV photon available for ionization becomes smaller while all of its energy is eventually converted into dust emission, resulting in a decrease of $L_{[\text{NII}]205}/L_{\text{IR}}$. On the other hand since the UV photon per dust particle increases, the dust temperature becomes higher, and then S_{63}/S_{158} becomes larger (Abel et al. 2009; Rigopoulou et al. 2018). Therefore, in both local and high-redshift galaxies, the decreasing trend can be explained by higher ionization parameters.

4.2 Oxygen line emission

Unlike $L_{[\text{NII}]205}/L_{\text{IR}}$, the photoionization models predicts increasing $L_{[\text{OIII}]88}/L_{\text{IR}}$ with increasing ionization parameter (Figure 3). This is because only a small fraction ($< 10\%$) of oxygen is doubly ionized at low ionization parameter. Nevertheless, local LIRGs do not show any correlation between $L_{[\text{OIII}]88}/L_{\text{IR}}$ and S_{63}/S_{158} . The $L_{[\text{OIII}]88}/L_{\text{IR}}$ values of two lensed SMGs (G09.83808 at $z = 6.0$ and SPT 0418-47 at $z = 4.2$; De Breuck et al. 2019) are also consistent with those in local LIRGs. From comparisons with photoionization models, we find that $L_{[\text{OIII}]88}/L_{\text{IR}}$ is very sensitive to a variation in age of star

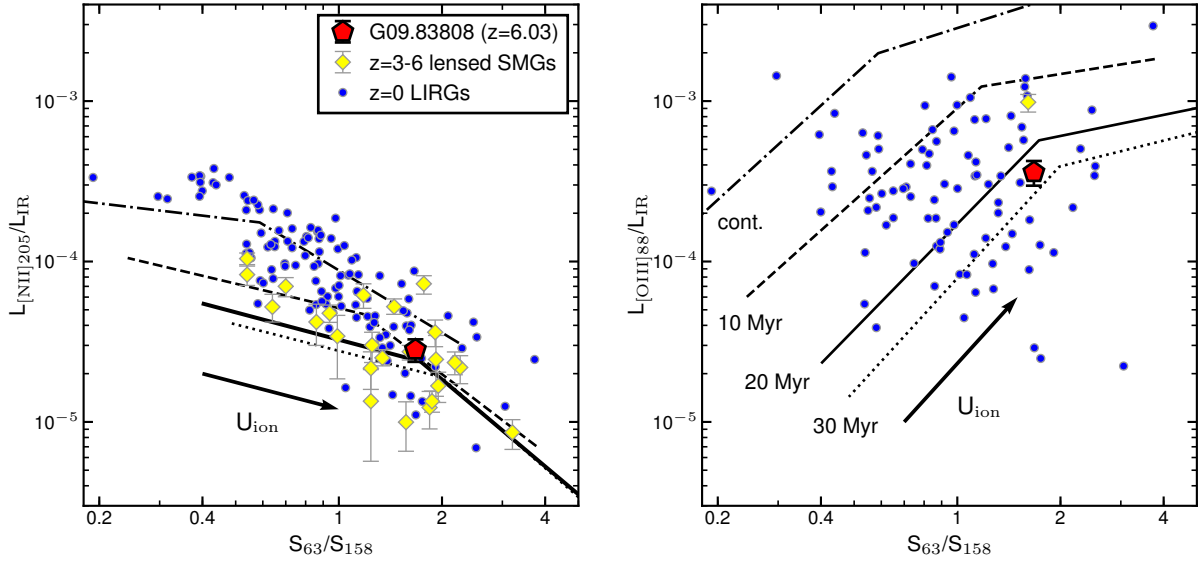


Fig. 3. Left: $[\text{N II}]_{205}$ line to infrared luminosity ratio as a function of S_{63}/S_{158} continuum ratio for local LIRGs and strongly-lensed SMGs. Right: $[\text{O III}]_{88}$ line to infrared luminosity ratios with the results from single starburst models with an age of 10, 20, and 30 Myr. A dashed dotted line show continuous star formation models with an age of 20 Myr. The ionization parameter varies from $U_{\text{ion}} = 10^{-4}$ to $U_{\text{ion}} = 10^{-2}$.

formation, which changes the energy distribution of incident radiation. The contribution of massive stars to the incident radiation is larger for ages younger than 20 Myr, leading to higher $L_{[\text{O III}]88}/L_{\text{IR}}$. The trend with changing age is almost orthogonal to the trend with changing ionization parameter. Therefore, the ionization parameter dependence of $L_{[\text{O III}]88}/L_{\text{IR}}$ quickly disappear due to a small variation in age of star formation. The impact of age variation on $[\text{N II}]_{205}$ is small because both trends are parallel in the $L_{[\text{N II}]205}/L_{\text{IR}}-S_{63}/S_{158}$ plane. Single starburst model with even the younger age (< 10 Myr) and continuous star formation models predict a much higher $L_{[\text{O III}]88}/L_{\text{IR}}$ of $10^{-3} - 10^{-2}$, which is similar to those in local dwarf galaxies (Cormier et al. 2015).

We also note that these arguments are based on simple spherical models in which all of $[\text{N II}]_{205}$, $[\text{O III}]_{88}$ and dust emissions are radiated from the same clouds. If $[\text{O III}]_{88}$ emission comes from a high density gas ($n_{\text{H}} > 1000 \text{ cm}^{-3}$) unlike $[\text{N II}]_{205}$, photoionization models with a different column density can reproduce a large variation in $L_{[\text{O III}]88}/L_{\text{IR}}$ ratio (Fischer et al. 2014).

5 Gas-phase metallicity

In this section, we estimate the gas-phase metallicity by using two measurements of $[\text{N II}]_{205}/[\text{O III}]_{88}$ and S_{63}/S_{158} ratio in G09.83808. Since $[\text{N II}]_{205}$ and $[\text{O III}]_{88}$ lines have different critical densities and ionization potential, its ratio depends not only on metallicity but also on gas density and ionization parameter. In lo-

cal LIRGs, the gas density is mostly in a narrow range of $n_{\text{e}}=20-100 \text{ cm}^{-3}$ (Díaz-Santos et al. 2017). We assume that the $z = 6$ galaxy has a line ratio of $\log(L_{[\text{N II}]122}/L_{[\text{N II}]205}) = 0.20 \pm 0.18$, which is the median value in LIRGs. This assumption is consistent with previous observations of SMGs at $z \sim 4$ (De Breuck et al. 2019; Lee et al. 2019). The ionization parameter dependence more seriously affects the estimates of metallicities when a $[\text{N II}]_{122}/[\text{O III}]_{88}$ line ratio is used. $[\text{N III}]_{57}/[\text{O III}]_{88}$ with similar ionization potential is considered to be a better indicator of metallicity (Nagao et al. 2011; Pereira-Santaella et al. 2017). However, either of $[\text{N III}]_{57}$ and $[\text{O III}]_{88}$ lines at $z > 6$ is shifted to be in frequency ranges where the atmospheric transmission is low or even zero, except for $z = 6.8 - 6.9$ and $z = 7.1 - 7.3$. In addition, as $[\text{N III}]_{57}$ emission at $z \sim 7$ can be observed with ALMA Band-9 receivers, the required integration time become by a factor of 60 larger than that in Band-7 observations of $[\text{N II}]_{122}$ line at the same limiting flux. An approach of using a $[\text{N II}]_{122}/[\text{O III}]_{88}$ line ratio therefore has a great advantage for future measurements of metallicity for a large sample once the dependence of the ionization parameter is taken into account.

In local galaxies where both lines are detected (Cormier et al. 2015; Fernández-Ontiveros et al. 2016; Herrera-Camus et al. 2018), the $[\text{N III}]_{57}/[\text{O III}]_{88}$ ratio is correlated with the $[\text{N II}]_{122}/[\text{O III}]_{88}$ ratio, though with a large dispersion (Figure 4). At a similar $[\text{N III}]_{57}/[\text{O III}]_{88}$ ratio, galaxies with a higher $[\text{N II}]_{122}/[\text{O III}]_{88}$ ratio tend to have a lower S_{63}/S_{158} ratio, corresponding to a lower ionization parameter.

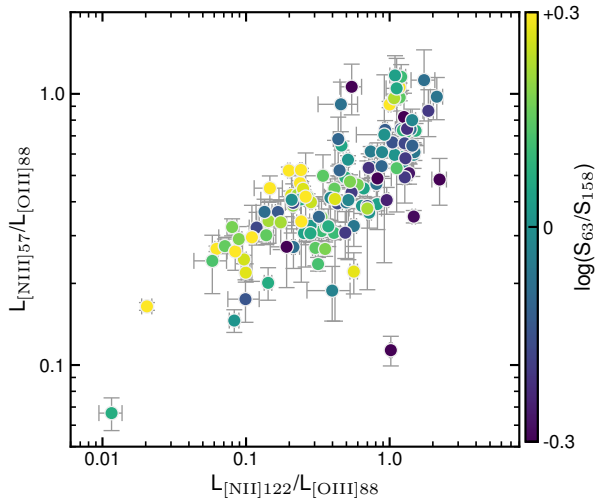


Fig. 4. A comparison between $L_{[\text{NII}]57}/L_{[\text{OIII}]88}$ and $L_{[\text{NII}]122}/L_{[\text{OIII}]88}$ for galaxies $z = 0$ (Cormier et al. 2015; Fernández-Ontiveros et al. 2016; Herrera-Camus et al. 2018). Color coding shows the S_{63}/S_{158} continuum ratio.

We therefore introduce the scaling relation to predict $[\text{N III}]_{57}/[\text{O III}]_{88}$ ratio as $\log(L_{[\text{NII}]57}/L_{[\text{OIII}]88})_{\text{pred}} = A + B \log(L_{[\text{NII}]205}/L_{[\text{OIII}]88}) + C \log(S_{63}/S_{158})$. We determine the coefficients to minimize the difference between the predicted and observed $[\text{N III}]_{57}/[\text{O III}]_{88}$ in local galaxies by ordinary least squares regression. Thus, we obtain $A = -0.21 \pm 0.02$, $B = 0.45 \pm 0.03$ and $C = 0.32 \pm 0.07$, with a dispersion of ± 0.14 dex in $\log(L_{[\text{NII}]57}/L_{[\text{OIII}]88})$.

By using the scaling relation, we infer $\log([\text{N III}]_{57}/[\text{O III}]_{88}) = -0.55 \pm 0.09$ where the uncertainty includes that due to the conversion from $[\text{N II}]_{205}$ to $[\text{N II}]_{122}$ as well as the measurement errors. This ratio is relatively low compared to local LIRGs (Figure 5), but implies $Z = 0.5 - 0.7 Z_{\odot}$ according to the photoionization models (section 4.1). Our result is consistent with previous studies, where it is claimed that SMGs at $z = 3 - 4$ are chemically evolved with nearly solar metallicity (e.g., Rigopoulou et al. 2018; Tadaki et al. 2019; De Breuck et al. 2019). Numerical simulations also predict $Z \sim 0.5 Z_{\odot}$ at $z = 6$ in the stellar mass range of $\log(M_{*}/M_{\odot}) = 10 - 10.5$ (Torrey et al. 2019). High-resolution 3–4 μm observations with the James Webb Space Telescope (JWST) will allow us to obtain the stellar mass of strongly-lensed galaxies at $z = 4 - 6$ in separate from a foreground object. Therefore, the ALMA–JWST synergetic observations will allow us to probe the massive end of stellar mass-metallicity relation for galaxies at $z = 6$, which has not been explored so far.

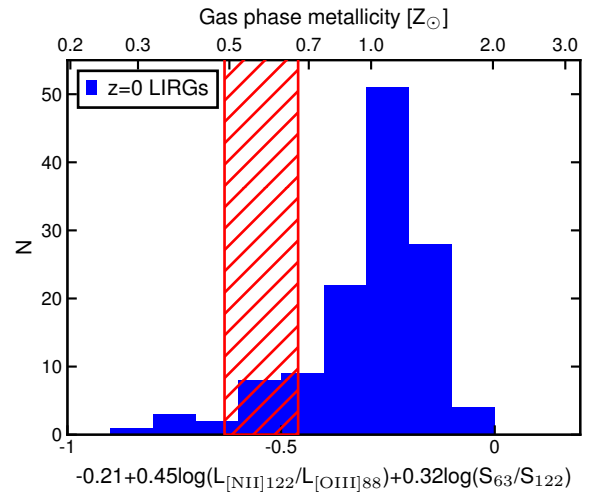


Fig. 5. A histogram of $[\text{N III}]_{57}/[\text{O III}]_{88}$ ratio inferred from the scaling relation for local LIRGs (blue; Díaz-Santos et al. 2017). A red hatched region shows the range of G09.83808 at $z = 6$, including uncertainties on conversion from $[\text{N II}]_{205}$ to $[\text{N II}]_{122}$. The top x-axis denotes gas-phase metallicities based on the photoionization models (section 4.1).

Acknowledgments

We thank the referee for constructive comments that improved the paper. We wish to thank Jacqueline Fischer for advice about photoionization modeling with *CLOUDY*. We also would like to thank Tanio Díaz-Santos and Rodrigo Herrera-Camus for kindly providing catalogs of galaxies at $z \sim 0$. This paper makes use of the following ALMA data: ADS/JAO.ALMA#2019.1.01307.S. ALMA is a partnership of ESO (representing its member states), NSF (USA) and NINS (Japan), together with NRC (Canada), MOST and ASIAA (Taiwan), and KASI (Republic of Korea), in cooperation with the Republic of Chile. The Joint ALMA Observatory is operated by ESO, AUI/NRAO and NAOJ. We thank the ALMA staff and in particular the EA-ARC staff for their support. This work was supported by JSPS KAKENHI Grant Numbers 20K14526, 17H06130. Data analysis was in part carried out on the Multi-wavelength Data Analysis System operated by the Astronomy Data Center (ADC), National Astronomical Observatory of Japan.

References

- Abel, N. P., Dudley, C., Fischer, J., Satyapal, S., & van Hoof, P. A. M. 2009, *ApJ*, 701, 1147
- Aihara, H., et al. 2019, *PASJ*, 71, 114
- Boquien, M., Burgarella, D., Roehly, Y., Buat, V., Ciesla, L., Corre, D., Inoue, A. K., & Salas, H. 2019, *A&A*, 622, A103
- Casey, C. M., et al. 2012, *ApJ*, 761, 140
- Cormier, D., et al. 2015, *A&A*, 578, A53
- Cowie, L. L., Songaila, A., Hu, E. M., & Cohen, J. G. 1996, *AJ*, 112, 839
- Crameri, F., Shephard, G. E., & Heron, P. J. 2020, *Nature Communications*, 11, 5444
- Cunningham, D. J. M., et al. 2020, *MNRAS*, 494, 4090
- De Breuck, C., et al. 2019, *A&A*, 631, A167
- Díaz-Santos, T., et al. 2017, *ApJ*, 846, 32

- Dudzevičiūtė, U., et al. 2020, MNRAS, 494, 3828
- Eldridge, J. J., & Stanway, E. R. 2016, MNRAS, 462, 3302
- Ferland, G. J., et al. 2017, RMxAA, 53, 385
- Fernández-Ontiveros, J. A., et al. 2016, ApJS, 226, 19
- Fischer, J., Abel, N. P., González-Alfonso, E., Dudley, C. C., Satyapal, S., & van Hoof, P. A. M. 2014, ApJ, 795, 117
- Fudamoto, Y., et al. 2017, MNRAS, 472, 2028
- Fujimoto, S., Ouchi, M., Kohno, K., et al. 2018, ApJ, 861, 7
- Glazebrook, K., et al. 2017, Nature, 544, 71
- Gullberg, B., et al. 2019, MNRAS, 490, 4956
- Herrera-Camus, R., et al. 2018, ApJ, 861, 94
- Hodge, J. A., et al. 2016, ApJ, 833, 103
- Ikarashi, S., et al. 2015, ApJ, 810, 133
- Iverson, R. J., et al. 2016, ApJ, 832, 78
- Kepley, A. A., Tsutsumi, T., Brogan, C. L., Indebetouw, R., Yoon, I., Mason, B., & Donovan Meyer, J. 2020, PASP, 132, 024505
- Kobayashi, C., Karakas, A. I., & Lugaro, M. 2020, ApJ, 900, 179
- Kubo, M., Tanaka, M., Yabe, K., Toft, S., Stockmann, M., & Gómez-Guijarro, C. 2018, ApJ, 867, 1
- Lee, M. M., et al. 2019, ApJL, 883, L29
- Li, J., et al. 2020, ApJ, 900, 131
- Lu, N., et al. 2017, ApJS, 230, 1
- Lutz, D., et al. 2016, A&A, 591, A136
- Marrone, D. P., et al. 2018, Nature, 553, 51
- McMullin, J. P., Waters, B., Schiebel, D., Young, W., & Golap, K. 2007, in *Astronomical Society of the Pacific Conference Series*, Vol. 376, *Astronomical Data Analysis Software and Systems XVI*, ed. R. A. Shaw, F. Hill, & D. J. Bell, 127
- Nagao, T., Maiolino, R., Marconi, A., & Matsuhara, H. 2011, A&A, 526, A149
- Novak, M., et al. 2019, ApJ, 881, 63
- Oguri, M. 2010, PASJ, 62, 1017
- Pavesi, R., Riechers, D. A., Faisst, A. L., Stacey, G. J., & Capak, P. L. 2019, ApJ, 882, 168
- Pereira-Santaella, M., Rigopoulou, D., Farrah, D., Leboutteiller, V., & Li, J. 2017, MNRAS, 470, 1218
- Riechers, D. A., et al. 2013, Nature, 496, 329
- Rigopoulou, D., Pereira-Santaella, M., Magdis, G. E., Cooray, A., Farrah, D., Marques-Chaves, R., Perez-Fournon, I., & Riechers, D. 2018, MNRAS, 473, 20
- Schreiber, C., et al. 2018, A&A, 618, A85
- Spilker, J. S., et al. 2016, ApJ, 826, 112
- Strandet, M. L., et al. 2016, ApJ, 822, 80
- Tadaki, K.-i., et al. 2019, ApJ, 876, 1
- Tadaki, K.-i., et al. 2020, ApJ, 901, 74
- Tamura, Y., Oguri, M., Iono, D., Hatsukade, B., Matsuda, Y., & Hayashi, M. 2015, PASJ, 67, 72
- Tanaka, M., et al. 2019, ApJL, 885, L34
- Thomas, D., Maraston, C., Schawinski, K., Sarzi, M., & Silk, J. 2010, MNRAS, 404, 1775
- Toft, S., et al. 2014, ApJ, 782, 68
- Torrey, P., et al. 2019, MNRAS, 484, 5587
- Valentino, F., et al. 2020, ApJ, 889, 93
- Weiß, A., et al. 2013, ApJ, 767, 88
- Zavala, J. A., et al. 2018, Nature Astronomy, 2, 56